Can we model the effect of observed sea level rise on tides?

Schindelegger, Michael; Green, Mattias; Wilmes, Sophie Berenice; Haigh, I.D.

Journal of Geophysical Research: Oceans

DOI:
10.1029/2018JC013959

Published: 05/07/2018

Peer reviewed version

Can we model the effect of observed sea level rise on tides?

M. Schindelegger[1], J. A. M Green[2], S-B. Wilmes[2,3], and I. D. Haigh[4]

[1]Institute of Geodesy and Geoinformation, University of Bonn, Bonn, Germany.
[2]School of Ocean Sciences, Bangor University, Menai Bridge, UK
[3]College of Earth, Ocean and Atmosphere Science, Oregon State University, Corvallis OR, USA
[4]Ocean and Earth Science, National Oceanography Centre Southampton, University of Southampton, Southampton, UK

Key Points:

- Effects of present-day sea level changes on global tides, primarily M_2, are studied using a non-linear barotropic model
- The model operates at high accuracy for its horizontal resolution and an explicit treatment of self-attraction and loading
- The sign of M_2 long-term trends is correctly simulated at 36 of 45 tide gauge stations

Corresponding author: M. Schindelegger, schindelegger@igg.uni-bonn.de

Abstract

The link between secular changes in the lunar semidiurnal ocean tide (M_2) and relative sea level rise (SLR) is examined based on numerical tidal modeling and the analysis of long-term sea level records from Europe, Australia, and the North American Atlantic coasts. The study sets itself apart from previous work by using a 1/12° global tide model that incorporates the effects of self-attraction and loading (SAL) through time step-wise spherical harmonic transforms instead of iteration. This novel SAL implementation incurs moderate computational overheads (some 50%) and facilitates the simulation of shelf sea tides with a global root mean square error of 14.6 cm in depths shallower than 1000 m. To reproduce measured tidal changes in recent decades, the model is perturbed with realistic water depth changes, compiled from maps of altimetric sea level trends and post-glacial crustal rebound. The M_2 response to the adopted SLR scenarios exhibits peak sensitivities in the North Atlantic and many marginal seas, with relative magnitudes of 1–5% per century. Comparisons with a collection of 45 tide gauge records reveals that the model reproduces the sign of the observed amplitude trends in 80% of the cases and captures considerable fractions of the absolute M_2 variability, specifically for stations in the Gulf of Mexico and the Chesapeake-Delaware Bay system. While measured-to-model disparities remain large in several key locations, such as the European Shelf, the study is deemed a major step toward credible predictions of secular changes in the main components of the ocean tide.

1 Introduction

Global mean sea level trends have recently been quantified at 1.2–1.7 mm yr^{-1} for the 20th century and at around 3.0 mm yr^{-1} since 1990 [*Ray and Douglas*, 2011; *Hay et al.*, 2015; *Hamlington and Thompson*, 2015; *Dangendorf et al.*, 2017]. This rise is far from being uniform in space [e.g., *Meyssignac and Cazenave*, 2012], with regional sea level changes reflecting the heterogeneous patterns of thermal expansion, air-sea interactions, ocean currents, and gravito-elastic responses to loss of land ice. Consensus exists that sea level rise (SLR) will remain unabated in the 21st century and beyond, most likely at rates exceeding those observed over the past few decades [*Church et al.*, 2013; *Goodwin et al.*, 2017, and references therein]. Amidst this commitment to SLR [*Goodwin et al.*, 2018], continued greenhouse gas emissions may initiate a full or partial collapse of the West Antarctic Ice Sheet with associated contributions to global sea levels of more than 1 m by 2100 and several meters a few centuries later [*DeConto and Pollard*, 2016]. While the major societal impacts of such sea level changes are due to coastal flooding and erosion—particularly during severe storms or high astronomical tides [*Ezer and Atkinson*, 2014]—increases in water depth may also alter bottom friction, wave propagation, and thus the tidal constituents themselves. Studies analyzing both global [*Woodworth*, 2010; *Müller et al.*, 2011] and regional sea level records [*Ray*, 2009; *Jay*, 2009; *Devlin et al.*, 2014; *Zaron and Jay*, 2014] have indeed found large-scale changes in diurnal and semi-diurnal constituents, reflected also in trends of tidal high water, low water and range [*Flick et al.*, 2003; *Mawdsley et al.*, 2014; *Mawdsley et al.*, 2015]. Understanding these long-term variations in terms of their physical origin is of scientific and practical importance, given that evolving tides will have repercussions for near-shore ecosystems, navigation, coastal protection, or tidal energy extraction. Yet, in most cases, linking the observed trends to sea level changes and other potential mechanisms has remained elusive.

With the gravitational forcing being virtually constant over the time span of the sea level records, measured trends in tidal amplitude and phase must be caused by local or large-scale oceanographic or terrestrial factors. Alongside SLR, processes of interest include [cf. *Woodworth*, 2010; *Müller*, 2012]: (i) natural or man-made morphological changes of coastal waters and estuaries, related to, e.g., variable river discharge rates [*Jay and Flinchem*, 1997] or dredging, (ii) changes in the generation of internal tides [*Colosi and Munk*, 2006], (iii) energy transfer between tidal constituents through resonant wave triads [*Lamb*, 2007], (iv) alterations in sea ice cover and mean currents, and (v) variable stratification with consequences for bottom friction and vertical viscosity [*Müller*, 2012]. Dependencies of the tides on sea level and/or basin shape changes have been explored in numerous computational studies, focusing on tidal adjustments since the Last Glacial Maximum [e.g., *Egbert et al.*, 2004; *Arbic et al.*, 2004; *Green*, 2010; *Wilmes and Green*, 2014] and under future sea level

increases on both global [e.g., *Pickering et al.*, 2017; *Wilmes et al.*, 2017] and regional scales [e.g., *Ward et al.*, 2012; *Pelling et al.*, 2013; *Luz Clara et al.*, 2015; *Carless et al.*, 2016]. However, attempts at validating and fine-tuning such integrations against the observational record of the past decades have been notoriously scarce. *Müller et al.* [2011] conducted comparisons of twentieth-century trends in tide gauge data with simulated responses to SLR and isostatic crustal motion but found poor agreement between their model predictions and the observations. This remains a troubling result, for it raises the questions of whether tidal projections to past and future conditions can be trusted.

To make progress, it is imperative to address and mitigate limitations of common numerical modeling techniques. Uncertainties in previous work on global tides have been in particular associated with the handling of gravitational feedbacks on tidal dynamics, collectively known as self-attraction and loading (SAL). Comparable to a tenth of the astronomical tide-raising force in magnitude and rich in spatial scales, the SAL term represents an order one influence on tides obtained through numerical methods [*Hendershott*, 1972]. How to include the effect in hydrodynamic equations is well-understood [e.g., *Gordeev et al.*, 1977; *Ray*, 1998] but non-trivial in practice; a complete treatment in forward models requires either global convolution integrals [*Farrell*, 1973; *Stepanov and Hughes*, 2004] or spherical harmonic transforms to be evaluated at each time step. While the latter approach has been shown to entail only moderate costs in coarse-resolution ($\sim 1°$) general circulation models [*Kuhlmann et al.*, 2011; *Vinogradova et al.*, 2015], explicit computation of SAL in forward mode is still deemed infeasible for tide models involving typical grid spacings of 10 km or less. Model iterations and offline convolutions have served as a frequent remedy instead [e.g. *Egbert et al.*, 2004]. Such solution strategies are however uneconomic and prone to slow convergence in shelf seas, thereby impairing the interpretation of modeled tidal responses to SLR [*Müller et al.*, 2011]. Progress toward accounting for SAL in a time step-wise (i.e., "online") fashion will thus pave the way for more accurate assessments of secular changes in ocean tides.

The paper is organized as follows. In Section 2, we describe the headways made in terms of numerical modeling. Realistic perturbations of the sea surface and the solid Earth-ocean interface are then adopted to deduce the trend patterns of global tides—primarily the M_2 constituent—in response to water depth changes representative of the past decades (Section 3). In Section 4, we validate the modeled M_2 variations with observed trends from the analysis of long-term tide gauge records in three different key regions. A brief look into future changes of the tide with a global sea level increase of 2 m is ventured in Section 5.

2 Hydrodynamic modeling

2.1 Model setup and validation

Codes from *Einšpigel and Martinec* [2017, see also http://geo.mff.cuni.cz/~einspigel/debot.html, accessed 14 June 2017] were adopted as time-domain solver of the non-linear shallow water equations with forcing from individual partial tides. Following up on earlier experiments [*Schindelegger et al.*, 2016], we have stripped down the model to its very core to prepare for inclusion of the full SAL machinery. Writing the undisturbed water depth as H, the tidal surface displacement with respect to the moving seafloor as ζ, and the corresponding velocity vector $\mathbf{u}$ as depth-integrated volume transport $\mathbf{U} = \mathbf{u}H$, the one-layer momentum and mass conservation equations read

$$\frac{\partial \mathbf{U}}{\partial t} + f \times \mathbf{U} + \nabla \cdot (\mathbf{U} \otimes \mathbf{u}) = -gH\nabla\left(\zeta - \zeta_{EQ} - \zeta_{SAL}\right) - \mathbf{F}_b - \mathbf{F}_w + a_H \nabla \cdot \boldsymbol{\sigma} \tag{1}$$

$$\frac{\partial \zeta}{\partial t} = -\nabla \cdot \mathbf{U} \tag{2}$$

where f is the Coriolis vector orientated along the local vertical, ∇ is the spherical del operator, $\otimes$ is the outer product, g denotes gravitational acceleration, ζ_{EQ} refers to the equilibrium tide [*Hendershott*, 1972], and ζ_{SAL} is the self-attraction and loading elevation. Energy is dissipated through a quadratic bed-friction term $\mathbf{F}_b = C_d \mathbf{U}|\mathbf{u}|/H$ (using $C_d = 3 \cdot 10^{-3}$ as dimensionless drag

coefficient) and a parameterized linear stress term $\mathbf{F}_w$ accounting for barotropic-to-baroclinic wave conversion over rough topography (discussed below). $a_H \nabla \cdot \boldsymbol{\sigma}$, with σ being a second-order tensor for Reynolds stress terms, introduces marginal additional friction due to horizontal eddy viscosity and prevents numerical instabilities in the presence of the non-linear advection terms in equation (1). The eddy viscosity coefficient itself ($a_H = 4 \cdot 10^2$ m^2 s^{-1}) is kept as small as grid resolution allows [*Egbert et al.*, 2004].

The model operates on a 1/12° finite difference grid running from 86°S to 84°N, with a somewhat coarser setup (1/8°) reserved for test purposes. Tidal elevations from a data-assimilative atlas [TPXO8 *Egbert and Erofeeva*, 2002, updated version] are prescribed at the open boundary in the Arctic Ocean and ramped up from zero over the first day of each integration. The bottom topography, used as basis for all simulations, was constructed from 1-minute RTOPO2 bathymetries [*Schaffer et al.*, 2016] (0.25 m vertical resolution) by forming average values for each computational grid cell and setting depths between 5 m and the 0-m isobath to 5 m. Water column depths under the Antarctic ice shelves are considered part of the ocean domain and readily computed from RTOPO2 maps of ice base and bedrock topography.

All model runs were forced with, and harmonically analyzed for, the leading diurnal and semidiurnal constituents M_2 and K_1. Of 17 days integration, 12 days are reserved for spin up, guaranteeing equilibration to within 0.5 mm in the open ocean and 2 mm in shelf areas excepting the Gulf of Carpentaria and the Sea of Okhotsk (not shown). Alongside the forced M_2 and K_1 constituents, energies are also generated in minor tidal bands through non-linearities in the equations of motion. We have thus augmented the harmonic fit at each grid point by two overtides (M_4, M_6) and one compound tide (MK_3).

With the main components of the model being standard choices, its performance with respect to altimetric tide solutions is essentially controlled by the adopted bathymetry and the internal tide drag parameterization $\mathbf{F}_w = C\mathbf{U}$. A large number of formulations for the conversion coefficient C is available [see *Green and Nycander*, 2013, and references therein]; here we use [*Zaron and Egbert*, 2006]

$$C(x, y) = \kappa_w \Gamma \left(\nabla H\right)^2 \frac{N_b \overline{N}}{8\pi^2 \omega} \tag{3}$$

in which $\Gamma = 50$ is a scaling factor, κ_w is our own independent tuning parameter, N_b is the observed buoyancy frequency at the ocean bottom, $\overline{N}$ is the vertical average of the observed buoyancy frequency, and ω represents the tidal frequency ($\omega = \omega_{M_2}$). Climatological mean fields of temperature and salinity were taken from the World Ocean Atlas 2013 version 2 [*Zweng et al.*, 2013] and converted to buoyancy frequencies on the native 1/4° data grid, with subsequent interpolation to the higher-resolution model grid. The drag scheme is activated for all depths, but values of $\overline{N}$ are set to zero in regions shallower than 100 m (assumed to be well-mixed).

Given the sea level focus here, κ_w is chosen in such a way that the model produces accurate M_2 elevations on a global scale. Simulated M_2 sinusoids $\hat{\zeta}$ (complex notation) were compared to the TPXO8 reference tide $\hat{\zeta}_R$ by evaluating the spatially averaged root mean square (RMS) errors $\overline{\Delta\zeta}$

$$\overline{\Delta\zeta} = \sqrt{\frac{\iint \left|\hat{\zeta} - \hat{\zeta}_R\right|^2 dA}{2 \iint dA}}$$

for areas deeper than 1000 m and equatorward of 66°. In approximate tuning experiments with strict consideration of SAL (see the next section), $\kappa_w = 0.3$ was found to yield $\overline{\Delta\zeta} = 4.4$ cm, equaling results of dedicated wave drag optimization efforts [*Buijsman et al.*, 2015]. For shallow shelf seas (depths < 1000 m), we obtain an RMS misfit relative to TPXO8 of $\overline{\Delta\zeta} = 14.6$ cm, significantly smaller than the shelf tide elevation error in any other existing forward model; cf. Table 12 in *Stammer et al.* [2014]. Comparisons with “ground truth" tidal estimates from 151 deep-ocean gauges and 195

shelf sea gauges [see *Stammer et al.*, 2014, for both datasets] yield reassuringly similar RMS results (5.9 cm and 14.2 cm, respectively). K_1 statistics with respect to TPXO8 are $\overline{\Delta\zeta} = 1.3$ cm in deep water and 4.8 cm in shallow areas. Figure 1 complements these global diagnostics by displaying local M_2 RMS discrepancies for our optimal 1/12° experiment using $\kappa_w = 0.3$. Fairly large elevation errors of 15–20 cm are seen in the North Atlantic, but in relative terms and on the European Shelf in particular, these discrepancies are generally within 15% of the tidal amplitude. The model lacks some fidelity in the seas around West Antarctica, most likely as a result of sparse observational constraints on stratification (and thus $\mathbf{F}_w$) in this region. We have been able to mitigate parts of these errors in additional test runs with basin-specific tuning of the tidal conversion [*Buijsman et al.*, 2015], but our final model configuration forgoes such optimizations.

2.2 Efficient time step-wise treatment of self-attraction and loading

Hendershott [1972]'s SAL formalism is based on a costly convolution of instantaneous water levels over the surface of the globe with a numerical Green's function. Here, as in studies by other authors [e.g., *Kuhlmann et al.*, 2011; *Vinogradova et al.*, 2015; *Irazoqui Apecechea et al.*, 2017], we adopt an efficient field approach that is only marginally less accurate than point-wise integrations [~ 3 mm error in complex coastal topographies; cf. *Schrama*, 2005]. Using spherical harmonics, convolution for SAL effects becomes a multiplication [*Ray*, 1998]

$$\zeta_{SAL,nm} = \frac{3\rho_w \left(1 + k'_n - h'_n\right)}{\rho_e \left(2n + 1\right)} \zeta_{nm} \tag{4}$$

where nm denotes degree and order of a particular spherical harmonic component, ρ_w and ρ_e are the mean densities of seawater and the Earth, and k'_n, h'_n are the degree-dependent load Love introduced by *Munk and MacDonald* [1960]. Note that the elevation field underlying this decomposition must be a global one, readily obtained in our code by adding M_2 and K_1 solutions from TPXO8 north of 84°N. The factor of proportionality $\left(1 + k'_n - h'_n\right)$ in equation (4) combines the three effects of SAL, which are, respectively, the direct gravitational attraction of water toward the load (i.e., the anomalous water mass), the deformation of the solid Earth under the oceanic tidal column (h'_n), and the potential perturbation induced by the load deformation (k'_n).

Implementing the physics of SAL in a forward model thus requires expansion of ζ into spherical harmonics, evaluation of equation (4)) in the spectral (wavenumber) domain, and transformation of $\zeta_{SAL,nm}$ to the model grid at each time step. The ζ_{SAL} field obtained thereof is then applied as additional surface load in the computation of horizontal velocities over the next time step. For global tide models at standard resolutions (≥1/8°) and correspondingly high degrees of expansion N, this spectral online approach is generally considered infeasible [e.g., *Müller et al.*, 2011; *Buijsman et al.*, 2015]. We challenge this view by exploiting advances in algorithm design for fast and accurate spherical harmonic transforms (SHT) documented in *Schaeffer* [2013]. Schaeffer's `SHTns` library achieves performance gains of order $O(10)$ over other third-party packages [e.g., SHTOOLS as employed by *Vinogradova et al.*, 2015], primarily through the usage of modern CPU vector capabilities and efficient on-the-fly evaluations of Legendre-associated functions for high degrees of truncation.

With `SHTns` requiring spatial data to be discretized on a regular Gaussian grid [e.g., *Hortal and Simmons*, 1991], we have interpolated water levels from the finite-difference grid in meridional direction, considering possible changes from dry to wet points (or vice versa) based on a high-resolution (1-minute RTOPO2) land-ocean mask. For our 1/12° runs, the expansion is taken to $N = 1079$ at each time step, equivalent to 1/6° horizontal resolution. SAL contributions from high wavenumbers ($N = 1080$ through 2159) are discarded, as those entail sea surface perturbations of less than a 1 mm bar a few estuaries and shelf areas. Finally, in evaluating equation (4), we have used Load Love numbers from *Wang et al.* [2012] with proper adjustments for degree 0 and 1 to be valid in the center of figure frame [*Blewitt*, 2003].

Table S1 in the supporting information presents results from timing experiments in which the classical scalar approximation $\zeta_{SAL} = \beta\zeta$, $\beta = const$. [*Accad and Pekeris*, 1978] is taken as reference. For our default configuration ($N = 1079$) on 8 computational threads, a full online treatment of SAL increases costs by ~ 0.10 s per time step, of which ~ 0.02 s are spent for regridding purposes. In relative terms, an overhead of only 51% is incurred, thus rendering any model iteration dispensable. Not unexpected, significant computational gains are achieved when the harmonic expansion is truncated at low degree, e.g., $N = 179$ corresponding to 1° grid resolution. This simplification—while of doubtful benefit for our studies of coastal waters—leaves M_2 errors in the open ocean below 1 mm.

We close this development section by a comparison of simulated M_2 amplitudes from our online SAL scheme and an iterative solution initialized by the scalar approximation $\zeta_{SAL} = 0.10\zeta$. To compensate for significantly longer runtimes in the presence of iterations, the model was configured on an ⅛° grid with slightly enhanced weight on the tidal conversion term ($\kappa_w = 0.5$). Five iterations were performed, and N was set to 719 for both online and offline SAL decompositions. M_2 amplitude differences in Figure 2 suggest that the somewhat canonical value of four iterations—adopted in many studies of changing tides and dissipation [*Müller et al.*, 2011; *Wilmes and Green*, 2014; *Pickering et al.*, 2017]—guarantees cm-accuracy in the open ocean but produces tidal solutions of less fidelity in many shelf seas. Residuals on the Patagonian Shelf (up to 6 cm) are large when compared to the projected M_2 changes in that area [*Carless et al.*, 2016], so additional iterations are required for better convergence. While a total of five SAL iterations emerge as optimal choice from Figure 2, we note that specific initialization measures [e.g., a spatially varying β-factor; cf. *Buijsman et al.*, 2015] and changes to the dissipation terms can lead to a vastly different behavior of the iteration process. Such dependencies limit the self-consistency of tidal simulations and are readily redressed by an explicit SAL decomposition at each time step.

3 Changes in relative sea level and global tides

3.1 Boundary conditions

With control runs completed, perturbations to the tide were prescribed in the form of relative SLR, i.e., changes to the height of the sea surface (absolute or geocentric sea level h) with respect to the Earth's crust c. For absolute sea level, we have adopted measured rates from AVISO's multi-mission altimetry product (http://www.aviso.oceanobs.com, accessed 21 August 2017) over the period 1993–2016 (Figure 3a). Note that an inverse barometer correction for atmospheric pressure loading is included in the AVISO processing protocol [*Ablain et al.*, 2009]. In evaluating $h(t) - c(t)$ over time t, allowance should be made for crustal motions associated with, e.g., tectonic processes, groundwater extraction, or the ongoing Glacial Isostatic Adjustment (GIA) to the ending of the last ice age. Direct and global observations of $c(t)$ do not exist, and many authors have thus omitted the term in their simulations of future tides [*Pelling and Green*, 2014; *Carless et al.*, 2016; *Pickering et al.*, 2017]. Here, we follow *Hall et al.* [2013] [see also *Egbert et al.*, 2004] and approximate crustal deformations with bathymetry predictions from GIA modeling to the exclusion of other, more local sources for radial movements of the crust. While admittedly incomplete, this treatment of $c(t)$ does lead to increasingly realistic estimates of water depth changes, which will be comparable to observations of relative sea level from tide gauges (Section 4).

The map of present-day rates of GIA-driven crustal motion (Figure 3b) is taken from ICE-6G_C [*Peltier et al.*, 2015], which incorporates constraints from relative sea level histories and space-geodetic measurements of vertical land motion in a best fit approach. Uplift of the crust occurs under the centers of the former Laurentide and Scandinavian ice sheets, while subsidence (and therefore relative sea level increase) is observed in peripheral region. Along the East Coast of North America—one of the primary regions of interest below—GIA particularly enhances relative sea levels through large subsidence rates on the order of -2 mm yr^{-1} [e.g., *Davis and Mitrovica*, 1996]. Owing to the far-field mechanisms of GIA [*Tamisiea and Mitrovica*, 2011], ICE-6G_C crust subsides at a mean rate of -0.22 mm yr^{-1} across all ocean basins, including the Arctic. In defining the time stamps of our bathymetry adjustments, we have thus added 0.22 mm yr^{-1} to the globally averaged

altimetry rate of 2.94 mm yr^{-1} (Figure 3a). The correction itself is at the lower-magnitude end of what is considered plausible from varying mantle viscosities and ice sheet histories [−0.15 mm yr^{-1} to −0.5 mm yr^{-1}; see *Tamisiea*, 2011]. Moreover, on regional scales, such as the North Atlantic, ICE-6G_C may not be sufficiently robust to serve as single best fit GIA model [*Roy and Peltier*, 2017; *Caron et al.*, 2018], implying the need for repeated tidal simulations with upper and lower bounds on isostatic crustal motion. Explorations of this kind and are presented in the supporting information [*Tamisiea*, 2011; *Caron et al.*, 2018].

With ICE-6G_C as primary crustal displacement model, projections of trend patterns in Figure 3 were made to sea level increases representative of the past decades, i.e., global averages of 0.1, 0.25, and 0.5 m. As waters rise, shorelines retreat and previously dry areas become inundated. How to deal with these occurrences at relatively wide grid spacings (∼10 km) is still a matter of some debate [*Pelling et al.*, 2013; *Pickering et al.*, 2017]. For sea level changes in the order of a few tens of cm, adding flooded cells with vertical extents of at least 5 m (model clipping depth) is a disproportionally large change in boundary conditions and may not be justified. Consequently, the simulations presented below were done with fixed land-ocean boundaries. The issue of inundation is revisited for larger sea level increases in Section 5.

3.2 Modeled tidal response

Tidal changes in our perturbation runs were found to be directly proportional to the imposed global mean sea level increase with a few isolated exceptions (Florida Bay, Skagerrak Strait in the North Sea). For clarity, we base our visualizations on the 0.5-m scenario. Figure 4a—along with corresponding regional close-ups (Figures 5 and 6)—suggests pronounced and alternating small-scale variations in M_2 amplitudes (∼2 cm, 1–5% in relative terms) across many shelf regions, for which the added relative sea level makes up a significant fraction of the overall water depth. In systems with natural periods close to the tidal forcing component, greater depths and associated increases in M_2 wavelength may alter tidal amplitudes through shifts in the resonance properties of the basin [*Müller et al.*, 2011; *Pickering et al.*, 2012]. Under no-flooding assumptions, the Gulf of Maine indeed approaches resonance with rising water levels, thereby enhancing the semi-diurnal tidal regime [*Pelling and Green*, 2013]. Conversely, diminished M_2 amplitudes on the Northwest Shelf of Australia indicate that the frequency disparity of the gulf and the tide in that region may increase. Contrasting views exist as to which tidal trends on the European Shelf relate to SLR-induced changes of the resonance state; cf. *Pelling et al.* [2013] and *Idier et al.* [2017]. The primary driver for M_2 increases in the Irish and Celtic Seas, the English Channel, and the German Bight appears to be a reduction of frictional dampening, for higher water levels entail weaker currents and bed shear stresses [*Ward et al.*, 2012; *Idier et al.*, 2017]. Particularly large M_2 responses in the Eastern Gulf of Mexico (∼6 cm) and the Delaware Bay are attributed to the same physical mechanism. Note that higher incoming wave amplitudes, altered reflection characteristics, and changes to the wavelength of the tide are also capable of shifting and intensifying amphidromic systems; see *Ross et al.* [2017] for a more detailed discussion.

Deep-ocean responses to SLR are weak in general (1–2 mm, possibly outside the model accuracy), yet a larger pattern of perturbations emerges in the Northwest Atlantic. The sensitivity of the tide to GIA in this area has been signified in previous explorations [Figure 11 of *Müller et al.*, 2011] and is emphasized in the present work through an additional forward integration with a globally uniform 0.5-m depth increase (Figure 4b). Evidently, in the absence of a glacial forebulge decay (at a rate of up to −6 mm yr^{-1}), much of the M_2 response in the deep North Atlantic switches sign and experiences attenuation. These results suggest that uniform SLR scenarios in future projections of tidal flooding [*Pickering et al.*, 2017] are not a fully adequate assumption and preferably replaced by spatially varying depth changes constrained by both the crust and the sea surface [*Hall et al.*, 2013; *Wilmes et al.*, 2017]. Adopting boundary conditions from AVISO and ICE-6G_C represents one such implementation; more sophisticated approaches might take into account uncertainties of GIA rates and absolute sea level maps with short-term regional variability (e.g., due to El Niño–Southern Oscillation) properly dampened [see Figure 21 of *Ray and Douglas*, 2011, for an example]. Both aspects are briefly addressed in the supporting information [Figures S2 and S3, based i.a. on *Tamisiea*,

2011; *Caron et al.*, 2018]. The sensitivity of M_2 changes to a Bayesian prediction spread of GIA models is marginal in most locations but appreciable in the Labrador Sea and the Gulf of Maine, with amplitude changes being as large as 5 mm for one standard deviation of GIA uplift rates. As we have not propagated these uncertainties to the simulation results below, some amount of caution is warranted when interpreting modeled tidal trends for Eastern North America.

A second experiment in the supporting information with uniform (instead of altimetric) geocentric sea level trends and the ICE-6G_C crust suggests M_2 changes that are almost identical to those in Figure 4a except for very shallow waters with above-average SLR (Eastern Gulf of Mexico, Seas of Indonesia, Arafura Sea), in which reduced frictional dissipation allows for larger tidal amplitudes. Such relevance of regionally intensified sea level rates also emerges for the K_1 constituent in the seas of Australasia (Figures 4c–4d). Little disparity is seen between uniform and non-uniform SLR runs as to the structure of the K_1 perturbation, yet the adoption of observed sea surface trends produces amplitude changes (up to 4.5 cm in the Gulf of Carpentaria) in considerable excess of the simulation with uniform depth increases. Enhanced or even accelerating sea level rates over certain shelf regions should thus be factored in when estimating future tides.

4 Comparing observed and modeled trends

4.1 Sea level data

Australia and the Atlantic coasts of Europe and North America, were selected for validation of the modeled M_2 response to SLR. A subset of some 150 potential stations—spread from Newfoundland to the Gulf of Mexico, from the North Sea to the Bay of Biscay, and along the seabed of Australia—was pinpointed in data archives from the Global Extreme Sea Level Analysis Version 2 [GESLA-2, *Woodworth et al.*, 2017] and the University of Hawaii Sea Level Center (UHSLC). Time series were adjusted for occasional spikes or data shifts and subsequently portioned in blocks of full calendar years having least 7000 hourly observations with individual data gaps being no longer than 20 days. To allow for an appropriate representation of the 18.61-year lunar nodal cycle [*Haigh et al.*, 2011], station records were required to span at least 28 years with a minimum of 15 calendar years of data within that period; cf. *Mawdsley et al.* [2015]. Many of the analyzed records contain data through the end of 2014, thereby guaranteeing sufficient overlap with the altimetry era. Special efforts were made to obtain an adequate run of sea levels for station Broome (Western Australia) using UHSLC data through the end of 2016.

At each of the TG stations, tidal and non-tidal residuals were separated from the longer-term mean sea level (MSL) component through application of a 4-day moving average with Gaussian weighting and a bell width of 0.5. Estimated trends in the tide appeared to be insensitive to the adopted smoothing technique as long as the cut-off period was kept in the sub-weekly band. Low-frequency filter residuals were averaged to annual values of MSL, while the high-frequency portion was subjected to independent tidal analysis for each calendar year using the Matlab® UTide software package [*Codiga*, 2011]. In trading off costs against accuracy, we have configured UTide for standard least squares, with an automated choice of constituents (typically 67) and confidence intervals computed from the colored residual spectra. M_2 amplitudes and phase lags obtained thereof were parameterized in terms of a mean value, a linear trend, a lag one-year autocorrelation, and two sinusoids (9.3 yr and 18.61 yr) to account for the exact nodal variations at each site; see *Ray* [2009] for further details. 95% confidence intervals from the UTide analysis were used to set up the weight matrix of the fit.

As a validation, M_2 regressions were performed for stations and time spans reported by *Woodworth* [2010]. In each case, trends in amplitude H and phase lag G were found to match Woodworth's results well within the formal errors. Yet, for many records with short duration or more erratic M_2 changes (e.g., Yarmouth, Nantucket, Cuxhaven), the choice of analysis windows exerts a considerable control on our final trend tabulations; cf. findings by *Ray* [2009]. To arrive at somewhat robust estimates, we have subjected the scatter of annual M_2 constants to visual consistency checks and repeated regression with varying start dates. This approach, though not a perfect remedy, discloses

outliers and chunks of suspicious tidal estimates that often mar the early parts of station time series. The example of Port Hedland (National Tidal Centre Australia) suffices here. Analysis of all available years (1966–2014) suggests a positive M_2 trend (0.34 ± 0.09 mm yr^{-1}), primarily constrained by amplitude estimates prior to a data gap from 1974 to 1984. Restriction to post-gap data (1985–2014) and times of greater SLR reverses the direction of the trend (-0.26 ± 0.06 mm yr^{-1}), thereby improving the agreement with station Broome and model simulations. We have also dismissed sites with statistically insignificant changes in amplitude (at 95% confidence).

In processing annual sea levels, adjustments were made for the 18.61-year equilibrium tide based on routines kindly provided by Richard Ray. Following our treatment of water column depth changes in Section 3.1, the GIA effect was retained in the observations as an integral part of crustal displacements. Initial regressions (of a linear trend and lag one-year autocorrelations) were carried out over the post-1980 period to assess the consistency with relative sea level rates in the simulations (Figure 4) and detect cases of (non-GIA) vertical land motion that would skew comparisons with model results. Large differences in local SLR, sometimes at the order of the signal itself (2–3 mm yr^{-1}), were found for stations Fishguard, Lerwick, Den Helder, Tregde, and tide gauges in the Gulf of Mexico. At credible sites, backward extensions were allowed for to the preferred tidal analysis windows (see previous paragraph; we use 1935 as the earliest starting point), as long as measured sea level trends and synthesized AVISO/GIA depth changes agreed within a factor of two. Upon application of all criteria, a fairly dense network of tide gauges was obtained in the northern US (Figure 5, 18 stations over the entire area), whereas parts of the European Shelf (Figure 6a, 15 stations) and Australia (Figure 6b, 12 stations) are somewhat undersampled.

4.2 Validation results

Figure 7 presents an initial validation in terms of response coefficients $r_H = \Delta H / \Delta s$, where ΔH denotes the change in tidal amplitude (in cm) and Δs represents the prescribed expansion of the water column (in m). For our trend simulation averaging 0.5 m depth increase, Δs is readily replaced by the corresponding GIA and altimetry rate ∂s upon nearest neighbor interpolation to the tide gauge site and application of a conversion factor $\eta = 0.5/3.16$ (in m mm^{-1} yr). Measured trends in tidal amplitude and relative sea level define the "ground truth" values of the response, i.e., $r_H = \partial H / \partial s$. Analogous expressions were adopted for the phase lags, G.

Across large parts of the domain, the model matches the observed spatial response to SLR, correctly accounting for the sign of the M_2 amplitude change at a total of 36 stations (80% of all cases). Exact trend values from tide gauges and simulations tend to differ by a factor of three to five, though, with disparities being particularly gross on the European Shelf (partly owing to reasons discussed below) and the entire East Coast of Australia, for which other mechanisms than SLR appear to act on the tides. Phase changes in the tide gauge data (Figure 7b) are insignificant at 15 stations and generally of little spatial coherence. The simulations, by contrast, imply shelf-wide phase decreases of up to $-20°$ (in the German Bight), consistent with the prevailing notion that higher water levels increase the celerity of the shallow water wave [*Idier et al.*, 2017].

Of all regions, the North Atlantic American Coast exhibits the closest agreement between observed and modeled M_2 trends; see also Figure 5. Amplitude and phase changes are especially well captured at Nantucket, in the Gulf of Mexico, and—to some extent—in the Chesapeake-Delaware Bay system. The realism of our global model in the latter area is of particular note, given that more sophisticated regional runs on unstructured meshes are thought to be required to reproduce the effects of friction and amphidromic adjustments on estuary tides; cf. *Ross et al.* [2017]. Negative amplitude responses to SLR at the mouth of the Delaware Bay are additionally worked out by a regression of annual M_2 changes (ΔH) against sea level changes (Δs) at station Lewes (1957–2014) in Figure 8. The plot suggests a good correlation between the two parameters, especially for recent times of higher water levels. Comparisons with model predictions from uniform and trend-SLR runs emphasize that the use of spatially varying depth changes is key to explaining secular trends of tides in that area.

Further north, in the Gulf of Maine, simulated response coefficients r_H are less than 20% of those inferred from observations; see the example of Portland in Figure 8. Inordinate water column

depth changes, such as a 2-m depression of Georges Bank, are needed to mimic the measured M_2 amplitude changes over the last decades [*Greenberg et al.*, 2012]. In experiments supplemental to those presented here, we have found that the Gulf of Maine response is moderately sensitive to bathymetry adjustments elsewhere, e.g., whether GIA-induced subsidence under the AVISO mask in Arctic latitudes were allowed for or not. This supports the conclusion of *Arbic et al.* [2009] that back effects may exist in a coupled shelf/deep-ocean system resonating at identical frequencies.

Evaluating the model performance on the European Shelf is complicated by the localized characteristics of several tide gauge sites. At Heysham and Delfzijl, silting issues have required periodic dredging, leading to significant interannual M_2 variability and large uncertainties of the estimated trends. Tidal amplitudes decreased linearly with rising sea levels at Lowestoft (Figure 8); the model fails to predict these changes, though, presumably due to the tide gauge's positioning beyond transversal breakwater structures that are not resolved on a $1/12^\circ$ grid. (In hindsight, such harbor geometries would have warranted exclusion.) In the Irish Sea and the German Bight—both characterized by a reduction in bed friction—the agreement between model and tide gauges is fairly good, even though the time series at Cuxhaven (1935–2014) exhibits large year-to-year fluctuations, possibly of meteorological origin (Figure 8). In the seas of Australia, the model captures the secular amplitude trends of the relatively small M_2 tide in Port Williams Bay (stations Williamstown and Geelong). Most notably, though, simulations with non-uniform SLR (5–6 mm yr^{-1} in the Eastern Indian Ocean) allow for an explanation of the long-term tidal changes at Broome and Port Hedland; see also Figure 8.

Given that disparities between observed and altimetry-constrained estimates of ∂H might skew the comparison in terms of response coefficients, we additionally validate the model results using relative amplitude and phase trends in Figure 9. These regressions are akin to Figures 12–13 in *Müller et al.* [2011] and evidence that our numerical model outperform any previous attempt to simulations the effect of SLR on tides. The plot gives emphasis to the close agreement between data and simulations for tide gauges with mean M_2 amplitudes in the order of a few tens of cm only, e.g., Lower Escuminac, Port Lincoln, Key West, and other annotated stations in Figure 9a. Concerning regional performance, the fit to observed M_2 changes is again best for tidal amplitudes along the North American coast, with magnitude differences for the resonant Gulf of Maine tides ranging from a factor of six (Yarmouth, Portland, Bar Harbor) to three at Boston [1.7% cy^{-1} observed vs. 0.6% cy^{-1} modeled, for comparison with *Ray*, 2009]. As above, results for stations in Europe and Australia are somewhat underwhelming and marred by individual outliers, yet the model produces the correct sign of the amplitude trend for all but seven stations in these regions. Regressions for tidal phases (Figure 9b) are far less encouraging, even though observations and model predictions consistently point to earlier arrival times of M_2 at approximately half of the stations. If condensed to a single global RMS value as a measure of the overall tidal variability, simulated amplitude trends are 66% of the RMS inferred from observations. Corresponding tabulations for the different regions are included in the supporting information [*Woodworth et al.*, 2017; *Ross et al.*, 2017] and bear out the marked improvement of our modeling results compared to those of *Müller et al.* [2011].

5 A glimpse of the future

Rigorous model validation, as in the previous section, provides context for tidal projections to more extreme mean sea level increases. Specifically, we have extrapolated relative sea level rates (Figure 3) to water depth changes averaging 2 m and derived M_2 solutions both for present-day coastal positions (no-flooding, NFL) and retreated shoreline (flooding, FL) scenarios [cf. *Pelling and Green*, 2014]. In constructing the FL depth chart, newly wetted cells were determined upon imposition of GIA/altimetry rates onto the 1-minute control bathymetry and subsequent averaging to $1/12^\circ$ with very shallow areas clipped to 5 m. Given that for runs with fixed coastlines (Section 3) sea level adjustments were made at $1/12^\circ$ resolution *after* clipping to minimal water depths, inconsistencies may be evoked between NFL and FL bathymetries at certain shallow offshore locations (e.g., in the southern parts of the North Sea). We have identified and corrected such cases during the construction of the FL depth chart; see *Pickering et al.* [2017] for a different approach.

Figure 10 illustrates semidiurnal tidal amplitude changes with respect to the control run for present-day conditions. In the open ocean, the two shoreline scenarios produce broadly consistent M_2 perturbations, even though flooding of new areas shifts the response toward increasingly negative values in many basins, particularly in the Weddell Sea and the Indian Ocean. Likewise, amplitude changes in the North Atlantic (e.g., Labrador Sea) are less pronounced in the FL case and bounded by M_2 decreases instead of increases (NFL) in the Subarctic. This result implies a northward shift of the amphidrome in the central North Atlantic, while eastward propagation is observed for sea level increases with invariant coastlines.

On a more local scale, the Gulf of Maine response for M_2 switches sign from +4 cm to −20 cm, which corresponds to the NFL/FL comparisons of *Pelling and Green* [2013]. The magnitude of that change is drastic, though, and most likely a repercussion of an improper discretization of the upper Bay of Fundy. Specifically, at SLR of 2 m, Minas Basin becomes amenable to tides for the first time in our model, dissipating significant amounts of energy through friction and thereby lowering tidal amplitudes in the rest of the Gulf. Further south, on the Patagonian Shelf, inundation is prevented by high cliffs [cf. *Luz Clara et al.*, 2015], yet the FL run displays a considerably larger sensitivity to SLR than simulations with unaltered present-day coastlines. This contradicts findings in *Carless et al.* [2016] and hints at feedback effects between shelf and basin tides, which are difficult to account for in numerical models configured for regional domains.

Figure 10 additionally highlights the impact of coastal recession on the European Shelf tide. If waters are allowed to inundate the low-lying shores of Denmark, Germany, and the Netherlands (unrealistic given the hard engineering in these locations), new centers of energy dissipation will be created and tidal ranges in the Southeast of the North Sea will be reduced. Movement of the entire North Sea amphidromic system to the newly introduced dissipative boundary conforms with expectations from process-based models of tidal wave propagation [*Rienecker and Teubner*, 1980; *Taylor*, 1921]. The exact mechanism appears to be a frictional loss in the incoming Kelvin wave, leaving less energy for the outbound wave propagating along the coast of continental Europe; see *Pelling et al.* [2013] and *Wilmes et al.* [2017] for a more comprehensive discussion. FL simulations in previous studies of the European Shelf [*Ward et al.*, 2012; *Pelling et al.*, 2013] fail to match our predictions of positive M_2 anomalies in the Northern North Sea as well as amplitude increases in the Irish and Celtic Seas. These local responses are common to both our FL and NFL simulations and corroborated by positive tide gauge trends at Smogen, Millport, Port Patrick, and Newlyn. In a tidal regime so sensitive to SLR, such observational constraints are precious, providing substance for future model improvements. The differences of our simulations with related work [e.g., *Pickering et al.*, 2012; *Pelling and Green*, 2014] suggest that revisiting regional tidal runs on the European Shelf with carefully chosen boundary conditions, spatially varying water depth changes, more recent bathymetric data bases, and a proper treatment of SAL would be a timely undertaking.

6 Discussion

Long-term variability of ocean tides is of major relevance for many coastal communities, with implications for flood risk management, navigation, tidal energy use, or the assessment of extreme water levels in engineering applications. Understanding and modeling such changes poses challenging technical and scientific problems. To advance the field, we have presented model simulations of enhanced robustness and resolution, yet still retaining a global focus, which is essential in accounting for the gravitational (SAL) feedbacks of instantaneous water masses and the far-field influences between shelf and basin tides. Emphasis has been on tidal changes of the more recent past and on carefully cross-checking numerical results with actual sea level records. This approach is evidently more conservative than recent research on the subject [e.g. *Pickering et al.*, 2017; *Idier et al.*, 2017; *Wilmes et al.*, 2017], as without validations for present-day conditions model projections to future times remain speculative at best. The primary result is that our simulations can reproduce the sign of the amplitude trends in most (80%) locations with significant changes in tides, thereby doing considerably better than previous studies of the topic [*Müller et al.*, 2011; *Pickering et al.*, 2017]. Moreover, magnitudes of observed and modeled M_2 trends are within a factor of four (or

less) from each other in nearly 50% of the considered cases. A tentative "Yes" or "Mostly" would therefore be the appropriate answer to the question posed in the title of the paper.

This conclusion may be not be valid in some specific locations, e.g., on the European Shelf or in the Gulf of Maine. Reconciling measurements and models in these areas is a multifaceted challenge. First, available observational records must be subject to further scrutiny and cleansed from spurious influences, such as dredging or port alterations [e.g., *Ross et al.*, 2017]. Complex harbor settings are to be treated with caution, given that signals obtained in these locations might not be representative of wider coastal sections. For tide modeling, higher resolution and accurate boundary conditions (that is, a detailed bathymetry and global charts of relative SLR) will be critical. In particular, the partial disagreement of in situ and AVISO/GIA-constrained depth changes (see Section 4.1) tells us that satellite-based sea surface trends, isostatic crustal adjustments, and estimates of vertical land motion [*Karegar et al.*, 2017] should be considered as joint factors in tidal projections.

The model presented here operates at unprecedented accuracy for its horizontal resolution [*Stammer et al.*, 2014] and is thus a suitable tool for investigating processes that may result in small changes, O(cm), of barotropic tidal elevations. We acknowledge, though, that alterations of the water column may not be the sole cause for secular variations in the ocean tide. Among the possible pathways for future modeling work, pursuing fully baroclinic tidal simulations with prescribed long-term changes of ocean stratification [*Müller*, 2012] seems a particularly worthwhile endeavor.

Acknowledgments
Financial support for this study was made available by the Austrian Science Fund (FWF, through project P30097-N29 of first author M.S.), the UK Natural Environmental Research Council (grants NE/F014821/1 and NE/I030224/1, J.A.M.G), and the National Science Foundation (grant OCE-1559153, S.W.B.). The sea level data came from UHSLC (https://uhslc.soest.hawaii.edu/data/) and GESLA-2 (www.gesla.org). All numerical simulations were performed using the Vienna Scientific Cluster (VSC). M_2 and K_1 charts for several SLR scenarios, along with corresponding solutions for the S_2 and O_1 constituents are available at https://www.gess.uni-bonn.de/daten-und-modelle/tides-SLR. We thank Kathy Quinn for her tutorial on SAL computations and David Einšpigel for providing an efficient tide modeling framework. Richard Ray acted both as reviewer and as swift provider of various datasets. Comments from a second reviewer greatly aided the geophysical discussion of the paper.

References

Ablain, M., A. Cazenave, G. Valladeau, and S. Guinehut (2009), A new assessment of the error budget of global mean sea level rate estimated by satellite altimetry over 1993–2008, *Ocean Sci.*, *5*, 193–201.

Accad, Y., and C. L. Pekeris (1978), Solution of the tidal equations for the M_2 and S_2 tides in the world oceans from a knowledge of the tidal potential alone, *Philos. Trans. R. Soc. London*, *290*, 235–266.

Arbic, B. K., D. R. Macayeal, J. X. Mitrovica, and G. A. Milne (2004), Palaeoclimate: ocean tides and Heinrich events, *Nature*, *432*, 460.

Arbic, B. K., R. H. Karsten, and C. Garrett (2009), On tidal resonance in the global ocean and the back-effect of coastal tides upon open-ocean tides, *Atmos.-Ocean*, *47*, 239–266, doi:10.3137/OC311.2009.

Blewitt, G. (2003), Self-consistency in reference frames, geocenter definition, and surface loading of the solid Earth, *J. Geophys. Res.*, *108*, 2103, doi:10.1029/2002JB002082, B2.

Buijsman, M. C., B. K. Arbic, J. A. M. Green, R. W. Helber, J. G. Richman, J. F. Shriver, P. G. Timko, and A. J. Wallcraft (2015), Optimizing internal wave drag in a forward barotropic model with semidurnal tides, *Ocean Modell.*, *85*, 42–55.

Carless, S. J., J. A. M. Green, H. E. Pelling, and S.-B. Wilmes (2016), Effects of future sea-level rise on tidal processes on the Patagonian Shelf, *J. Marine Syst.*, *163*, 113–124.

Caron, L., E. R. Ivins, E. Larour, S. Adhikari, J. Nilsson, and G. Blewitt (2018), GIA model statistics for GRACE hydrology, cryosphere, and ocean science, *Geophys. Res. Lett.*, *45*, 2203–2212, https://doi.org/10.1002/2017GL076644.

Church, J. A., et al. (2013), Sea Level. Climate Change 2013, In: Stocker T. F., Qin D., Plattner G.-K., Tignor M., Allen S. K., Boschung J., Nauels A., Xia Y., Bex V., and Midgley P.M. (eds.), *The Physical Science Basis. Contribution of Working Group I to the Fifth Assessment Report of the Intergovernmental Panel on Climate Change*, pp. 1137–1216, Cambridge University Press, Cambridge, UK, and New York, NY, USA, doi:10.1017/ CBO9781107415324.026.

Codiga, D. L. (2011), Unified tidal analysis and prediction using the UTide Matlab functions, Technical Report 2011-01, Graduate School of Oceanography, University of Rhode Island Narragansett, RI, doi:10.13140/RG.2.1.3761.2008.

Colosi, J. A., and W. Munk (2006), Tales of the venerable Honolulu tide gauge, *J. Phys. Oceanogr.*, *36*, 967–996.

Dangendorf, S., M. Marcos, G. Wöppelmann, C. P. Conrad, T. Frederikse, and R. Riva (2017), Reassessment of 20th century global mean sea level rise, *P. Natl. Acad. Sci. USA*, *114*, 5946–5951.

Davis, J. L., and J. X. Mitrovica (1996), Glacial isostatic adjustment and the anomalous tide gauge record of eastern North America, *Nature*, *379*, 331–333, doi:10.1038/379331a0.

DeConto, R. M., and D. Pollard (2016), Contribution of Antarctica to past and future sea-level rise, *Nature*, *531*, 591–600.

Devlin, A. T., D. A. Jay, S. A. Talke, and E. D. Zaron (2014), Can tidal perturbations associated with sea level variations in the western Pacific Ocean be used to understand future effects of tidal evolution?, *Ocean Dynam.*, doi:10.1007/s10236-014-0741-6:1-28.

Egbert, G. D., and S. Y. Erofeeva (2002), Efficient inverse modeling of barotropic ocean tides, *J. Atmos. Ocean. Technol.*, *19*, 183–204.

Egbert, G. D., R. D. Ray, and B. G. Bills (2004), Numerical modeling of the global semidiurnal tide in the present day and in the last glacial maximum. *J. Geophys. Res.*, *109*, C03003, doi:10.1029/2003JC001973.

Einšpigel, D., and Z. Martinec (2017), Time-domain modeling of global ocean tides generated by the full lunisolar potential, *Ocean Dynam.*, *67*, 165–189, doi:10.1007/s10236-016-1016-1.

Ezer, T., and L. P. Atkinson (2014), Accelerated flooding along the U.S. East Coast: On the impact of sea-level rise, tides, storms, the Gulf Stream, and the North Atlantic Oscillations, *Earth's Future*, *2*, 362–382. doi:10.1002/2014EF000252.

Farrell, W. E. (1973), Earth tides, ocean tides, and tidal loading, *Philos. Trans. R. Soc. Lond. A*, *274*, 253–259.

Flick, R., J. Murray, and L. Ewing (2003), Trends in United States tidal datum statistics and tide range, *J. Waterw. Port Coastal Ocean Eng.*, *129*, 155–164.

Goodwin, P., I. D. Haigh, E. J. Rohling, and A. Slangen (2017), A new approach to projecting 21st century sea-level changes and extremes, *Earth's Future*, *5*, 240–253. doi:10.1002/2016EF000508.

Goodwin, P., S. Brown, I. D. Haigh, R. J. Nicholls, and J. M. Matter (2018), Adjusting mitigation pathways to stabilize climate at 1.5 and 2.0° in global temperatures to year 2300, *Earth's Future*, *6*, 601–615, doi:https://doi.org/10.1002/2017EF000732.

Gordeev, R. G., B. A. Kagan, and E. V. Polyakov (1977), The effects of loading and self-attraction on global ocean tides: The model and the results of a numerical experiment, *J. Phys. Oceanogr.*, *7*, 161–170.

Green, J. A. M. (2010), Ocean tides and resonance, *Ocean Dynam.*, *60*(5), 1243–1253, doi:10.1007/s10236-010-0331-1.

Green, J. A. M., and J. Nycander (2013), A comparison of tidal conversion parameterizations for tidal models, *J. Phys. Oceanogr.*, *43*, 104–119, doi:10.1175/JPO-D-12-023.1.

Greenberg, D. A., W. Blanchard, B. Smith, and E. Barrow (2012), Climate change, mean sea level and high tides in the Bay of Fundy, *Atmos.-Ocean*, *50*, 261–276, doi:10.1080/07055900.2012.668670.

Haigh, I. D., M. Eliot, and C. Pattiaratchi (2011), Global influences of the 18.61 year nodal cycle and 8.85 year cycle of lunar perigee on high tidal levels, *J. Geophys. Res.*, *116*, C06025, doi:10.1029/2010JC006645.

Hall, G. F., D. F. Hill, B. P. Horton, S. E. Engelhart, and W. R. Peltier (2013), A high-resolution study of tides in the Delaware Bay: Past conditions and future scenarios, *Geophys. Res. Lett.*, *40*, 338–242, doi:10.1029/2012GL054675.

Hamlington, B. D., and P. R. Thompson (2015), Considerations for estimating the 20th century trend in global mean sea level, *Geophys. Res. Lett.*, *42*, 4102–4109, doi:10.1002/2015GL064177.

Hay, C. C., E. Morrow, R. E. Kopp, and J. X. Mitrovica (2012), Probabilistic reanalysis of twentieth-century sea-level rise, *Nature*, *517*, 481–484, doi:10.1038/nature14093.

Hendershott, M. C. (1972), The effects of solid earth deformations on global ocean tides, *Geophys. J. R. Astron. Soc.*, *29*, 389–402.

Hortal, A., and A. J. Simmonds (1991), Use of reduced Gaussian grids in spectral models, *Mon. Weather Rev.*, *119*, 1057–1074.

Idier, D., F. Paris, G. L. Cozannet, F. Boulahya, and F. Dumas (2017), Sea-level rise impacts on tides of the European Shelf, *Cont. Shelf Res.*, *137*, 56–71.

Irazoqui Apecechea, M., M. Verlaan, F. Zijl, C. Le Coz, and H. Kernkamp (2017), Effects of self-attraction and loading at a regional scale: a test case for the Northwest European Shelf, *Ocean Dynam.*, *67*, 729–749, doi:10.1007/s10236-017-1053-4.

Jay, D. A. (2009), Evolution of tidal amplitudes in the eastern Pacific Ocean, *Geophys. Res. Lett.*, *36*, L04603, doi:10.1029/2008GL036185.

Jay, D. A., and E. P. Flinchem (1997), Interaction of fluctuating river flow with a barotropic tide: A demonstration of wavelet tidal analysis methods, *J. Geophys. Res.*, *102*, C3, 5705–5720, doi:10.1029/2008GL036185.

Karegar, M. A., T. H. Dixon, R. Malservisi, J. Kusche, and S. E. Engelhart (2017), Nuisance flooding and relative sea-level rise: the importance of present-day land motion, *Sci. Rep.*, *7*, 11197, doi:10.1038/s41598-017-11544-y.

Kuhlmann, J., H. Dobslaw, and M. Thomas (2011), Improved modeling of sea level patterns by incorporating self-attraction and loading, *J. Geophys. Res.*, *116*, C11036, doi:10.1029/2011JC007399.

Lamb, K. G. (2007), Tidally generated near-resonant internal wave triads at a shelf break, *Geophys. Res. Lett.*, *34*, L18607, doi:10.1029/2007GL030825.

Luz Clara, M., C. G. Simionato, E. D'Onofrio, and D. Moreira (2015), Future sea level rise and changes on tides in the Patagonian Continental Shelf, *J. Coastal Res.*, *313*, 519–535, doi:10.2112/JCOASTRES-D-13-00127.1.

Mawdsley, R. J., I. D. Haigh, and N. C. Wells (2014), *Global changes in tidal high water, low water and range*, In: Green, A.N. and Cooper, J.A.G. (eds.), Proceedings 13th International Coastal Symposium (Durban, South Africa), *J. Coastal Res.*, *70*, 343–348.

Mawdsley, R. J., I. D. Haigh, and N. C. Wells (2015), Global secular changes in different tidal high water, low water and range levels, *Earth's Future*, *3*, 66–81. doi:10.1002/2014EF000282

Meyssignac, B., and A. Cazenave (2012), Sea level: A review of present-day and recent-past changes and variability, *J. Geodyn.*, *58*, 96–109, doi:10.1016/j.jog.2012.03.005.

Müller, M. (2012), The influence of changing stratification conditions on barotropic tidal transport and its implications for seasonal and secular changes of tides, *Cont. Shelf. Res.*, *47*, 107–118.

Müller, M., B. Arbic, and J. Mitrovica (2011), Secular trends in ocean tides: Observations and model results, *J. Geophys. Res.*, *116*, C05013, doi:10.1029/2010JC006387.

Munk W. H., and G. J. F. MacDonald (1960), *The Rotation of the Earth: A Geophysical Discussion*, Cambridge University Press, New York.

Pelling, H. E., and J. A. M. Green (2013), Sea level rise and tidal power plants in the Gulf of Maine, *J. Geophys. Res. Oceans*, *118*, 2863–2873, doi:10.1002/jgrc.20221.

Pelling, H. E., J. A. M. Green, and S. L. Ward (2013), Modelling tides and sea-level rise: To flood or not to flood, *Ocean Modell.*, *63*, 21–29.

Pelling, H. E., and J. A. M. Green (2014), Impact of flood defences and sea-level rise on the European Shelf tidal regime, *Cont. Shelf Res.*, *85*, 96–105.

Peltier, W. R., D. F. Argus, and R. Drummond (2015), Space geodesy constrains ice age terminal deglaciation: The global ICE-6G_C (VM5a) model, *J. Geophys. Res. Solid Earth*, *120*, 450–487, doi:10.1002/2014JB011176.

Pickering, M. D., N. C. Wells, K. J. Horsburgh, and J. A. M. Green (2012), The impact of future sea-level rise on the European Shelf tides, *Cont. Shelf Res.*, *35*, 1–15.

Pickering, M. D., K. J. Horsburgh, J. R. Blundell, J. J.-M. Hirschi, R. J. Nicholls, M. Verlaan, and N. C. Wells (2017), The impact of future sea-level rise on the global tides, *Cont. Shelf Res.*, *142*, 50–68.

Ray, R. D. (1998), Ocean self-attraction and loading in numerical tidal models, *Mar. Geod.*, *21*, 181–192.

Ray, R. D. (1998), Secular changes in the solar semidiurnal tide of the western North Atlantic Ocean, *Geophys. Res. Lett.*, *36*, L19601, doi:10.1029/2009GL040217.

Ray, R. D., and B. C. Douglas (2011), Experiments in reconstructing twentieth-century sea levels, *Prog. Oceanogr.*, *91*, 496–515.

Rienecker, M., and M. Teubner (1980), A note on frictional effects in Taylor's problems, *J. Mar. Res.*, *38*, 183–191.

Ross, A. C., R. G. Najar, M. Li, S. B. Lee, F. Zhang, and W. Liu (2017), Fingerprints of sea level rise on changing tides in the Chesapeake and Delaware Bays, *J. Geophys. Res. Oceans*, *122*, 8102–8125, doi:10.1002/2017JC012887.

Roy, K., and W. R. Peltier (2017), Space-geodetic and water level gauge constraints on continental uplift and tilting over North America: Regional convergence of the ICE-6G_C (VM5a/VM6) models, *Geophys. J. Int.*, *210*, 1115–1142.

Schaeffer, N. (2013), Efficient spherical harmonic transforms aimed at pseudospectral numerical simulations, *Geochem. Geophys. Geosyst.*, *14*, 751–758, doi:10.1002/ggge.20071.

Schaffer, J., R. Timmermann, J. E. Arndt, S. Savstrup Kristensen, C. Mayer, M. Morlighem, and D. Steinhage (2016), A global, high-resolution data set of ice sheet topography, cavity geometry, and ocean bathymetry, *Earth Syst. Sci. Data*, *8*, 543–557, doi:10.5194/essd-8-543-2016.

Schindelegger, M., D. Einšpigel, D. Salstein, and J. Böhm (2016), The global S_1 tide in Earth's nutation, *Surv. Geophys.*, *37*, 643–680, doi:10.1007/s10712-016-9365-3.

Schrama, E. J. O. (2005), Three algorithms for the computation of tidal loading and their numerical accuracy, *J. Geod.*, *78*, 707–714.

Stammer, D., et al. (2014), Accuracy assessment of global barotropic ocean tide models, *Rev. Geophys.*, *52*, 243–282, doi:10.1002/2014RG000450.

Stepanov, V. N., and C. W. Hughes (2004), Parameterization of ocean self-attraction and loading in numerical models of the ocean circulation, *J. Geophys. Res.*, *109*, C07004, doi:10.1029/2003JC002034.

Tamisiea, M. E. (2011), Ongoing glacial isostatic contributions to observations of sea level change, *Geophys. J. Int.*, *186*, 1036–1044, doi:10.1111/j.1365-246X.2011.05116.x.

Tamisiea, M. E., and J. X. Mitrovica (2011), The moving boundaries of sea level change: Understanding the origins of geographic variability, *Oceanography*, *24*, 24–39.

Taylor, G. I. (1921), Tidal oscillations in gulfs and rectangular basins, *P. Lond. Math. Soc.*, *20*, 148–181,

Vinogradova, N. T., R. M. Ponte, K. J. Quinn, M. E. Tamisiea, J.-M. Campin, and J. L. Davis (2015), Dynamic adjustment of the ocean circulation to self-attraction and loading effects, *J. Phys. Oceanogr.*, *45*, 678–689, doi:10.1175/JPO-D-14-0150.1.

Wang, H., L. Xiang, L. Jia, L. Jiang, Z. Wang, B. Hu, and P. Gao (2012), Load Love numbers and Green's functions for elastic Earth models PREM, iasp91, ak135, and modified models with refined crustal structure from Crust 2.0, *Comp. Geosci.*, *49*, 190–199.

Ward, S. L., J. A. M. Green, and H. E. Pelling (2012), Tides, sea-level rise and tidal power extraction on the European shelf, *Ocean Dynam.*, *62*, 1153–1167, doi:10.1007/s10236-012-0552-6.

Wilmes, S.-B., and J. A. M. Green (2014), The evolution of tides and tidal dissipation over the past 21,000 years, *J. Geophys. Res. Oceans*, *119*, 4083–4100, doi:10.1002/2013JC009605.

Wilmes, S.-B., J. A. M. Green, N. Gomez, T. P. Rippeth, and H. Lau (2017), Global tidal impacts of large-scale ice-sheet collapses, *J. Geophys. Res. Oceans*, *122*, 8354–8370, doi:10.1002/2017JC013109.

Woodworth, P. L. (2010), A survey of recent changes in the main components of the ocean tide, *Cont. Shelf Res.*, *30*, 1680–1691.

Woodworth, P. L., J. R. Hunter, M. Marcos, P. Caldwell, M. Menendez, and I. Haigh (2017), Towards a global higher-frequency sea level data set, *Geosci. Data J.*, *3*, 50–59, doi:10.1002/gdj3.42.

Zaron, E. D., and D. A. Jay (2014), An analysis of secular change in tides at open-ocean sites in the Pacific, *J. Phys. Oceanogr.*, *44*, 1704–1726.

Zaron, E. D., and G. D. Egbert (2006), Estimating open-ocean barotropic tidal dissipation: The Hawaiian Ridge, *J. Phys. Oceanogr.*, *36*, 1019–1035.

Zweng, M. M. et al. (2013), World Ocean Atlas 2013, Volume 2: Salinity, In: Levitus S., Mishonov A. (eds.) *NOAA Atlas NESDIS 74*, 39 pp., Silver Spring, MD.

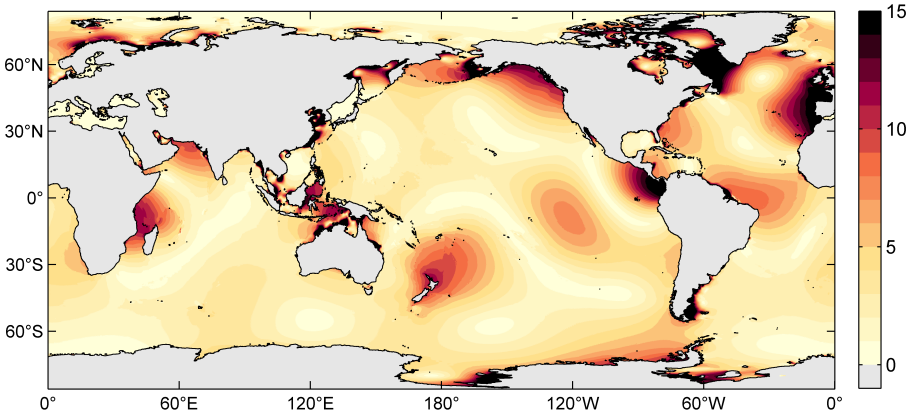

Figure 1. M_2 RMS elevation error (cm) between the TPXO8 atlas and our $1/12^\circ$ simulations based on online evaluation of SAL and a scale factor of $\kappa_w = 0.3$ applied to the conversion scheme. Corresponding global-mean RMS errors are 4.4 cm for depths greater than 1000 m and 14.6 cm in shallow oceans.

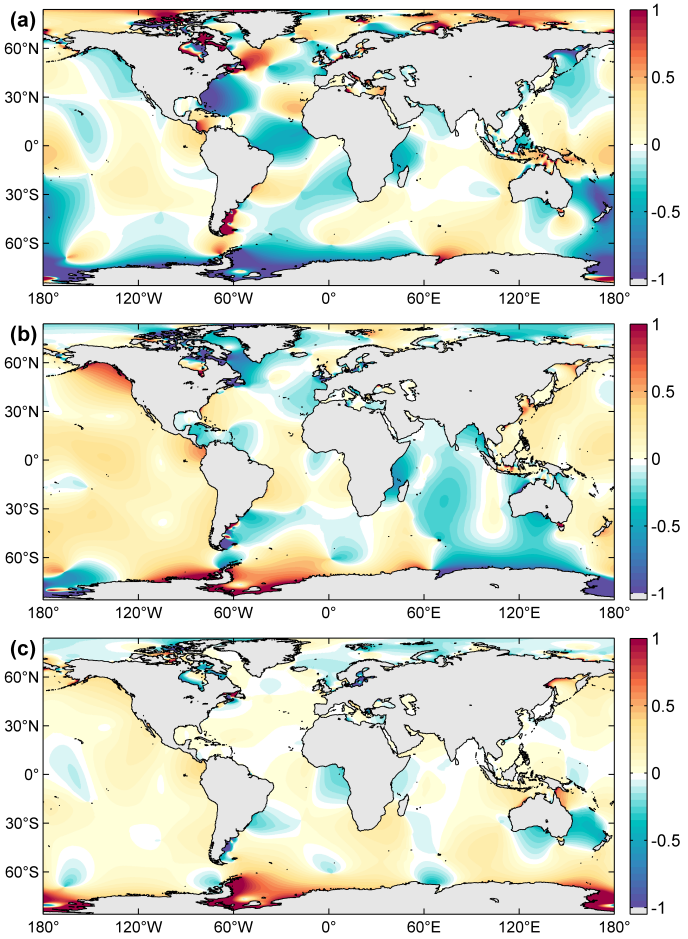

Figure 2. Difference in M_2 amplitudes (cm) between the SAL-online control run and an iterating simulation initialized by $\beta = 0.10$. Panels show differences after (a) three, (b) four, and (c) five iterations. As in *Egbert et al.* [2004], the iterative procedure employs a memory term for rapid convergence. Global-mean RMS errors in deep (shallow) water are 5.1 cm (17.0 cm) for the control run and 5.1 cm (17.1 cm) after five iterations.

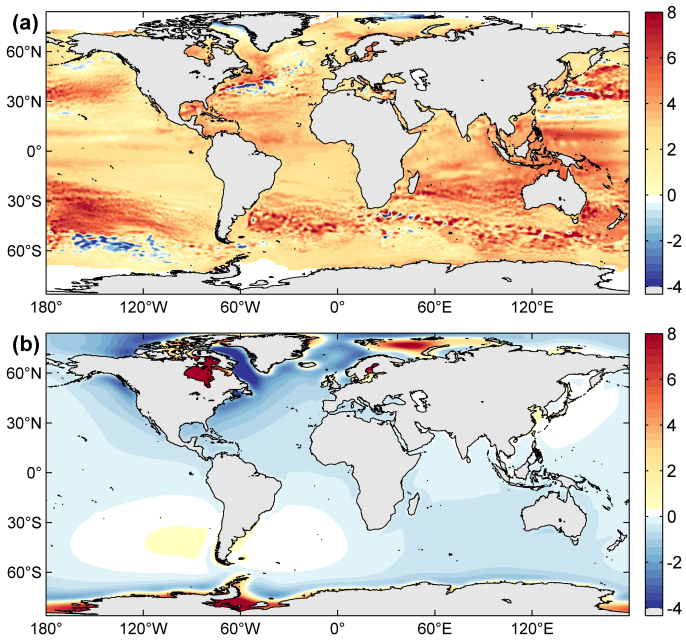

Figure 3. Trend patterns (mm yr^{-1}) showing changes in water depth: (a) geocentric sea level trends measured by altimetry and (b) GIA-induced crustal motions from ICE-6G_C.

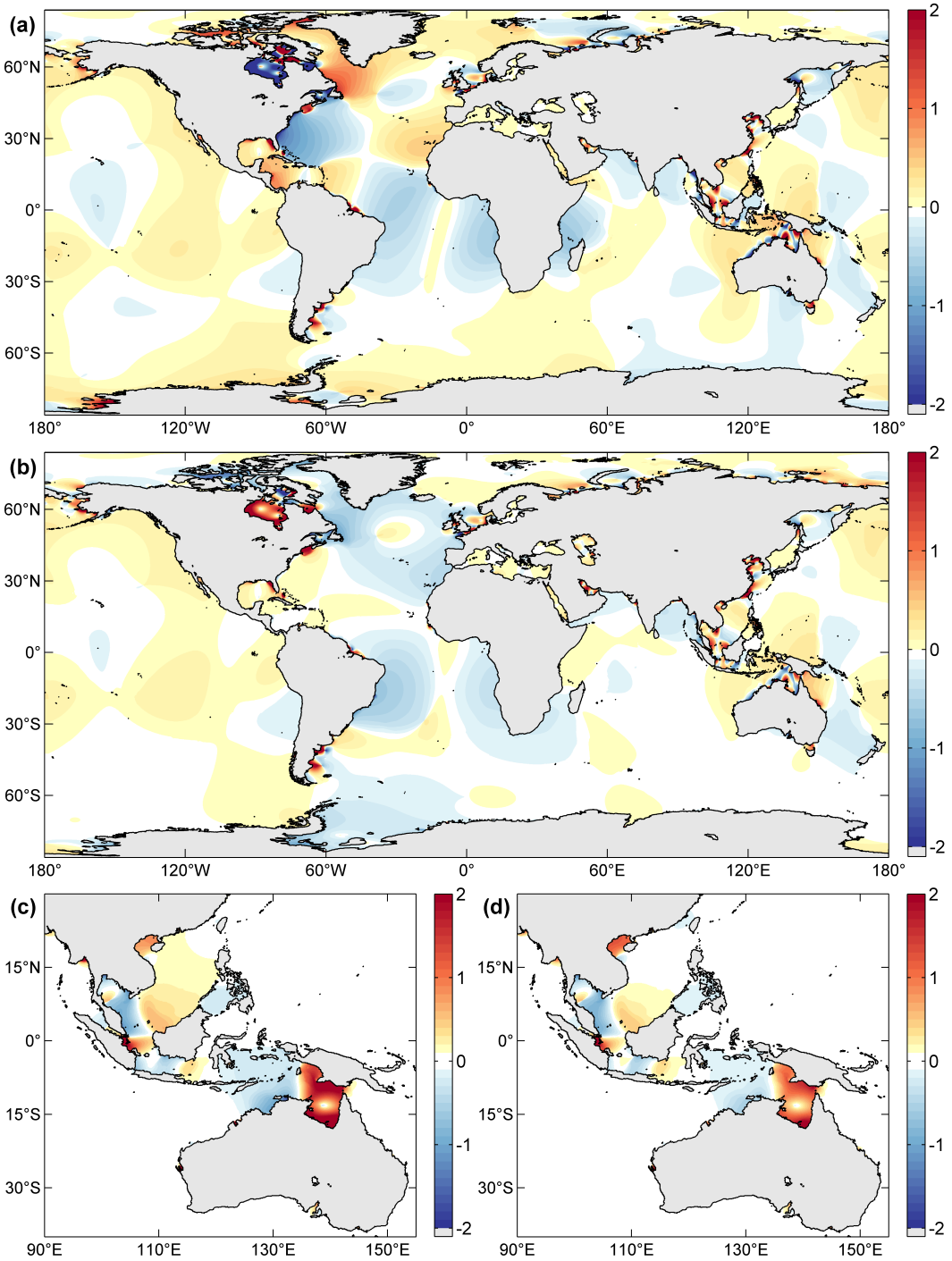

Figure 4. Modeled response of M_2 (a,b) and regional K_1 (c,d) tidal amplitudes (cm) to a 0.5 m increase in global mean sea level based on two different scenarios: (a,c) non-uniform SLR with GIA and eustatic trends extrapolated from Figure 3, and (b,d) spatially uniform SLR.

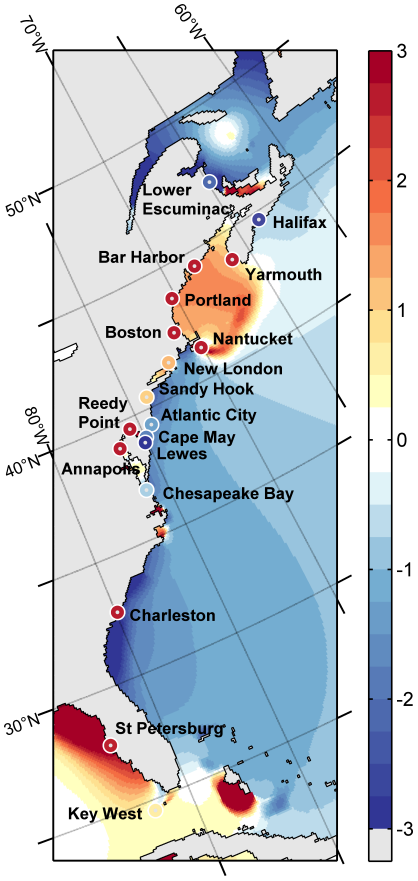

Figure 5. Close-up of Figure 4a for M_2 tidal amplitude changes (cm) along the North American East Coast, including 18 of 45 tide gauge stations used in this study. Circles at the tide gauge sites are color-coded to represent the measured M_2 changes (reckoned as response coefficients in cm per 0.5-m of SLR; see Section 4.2 for more information).

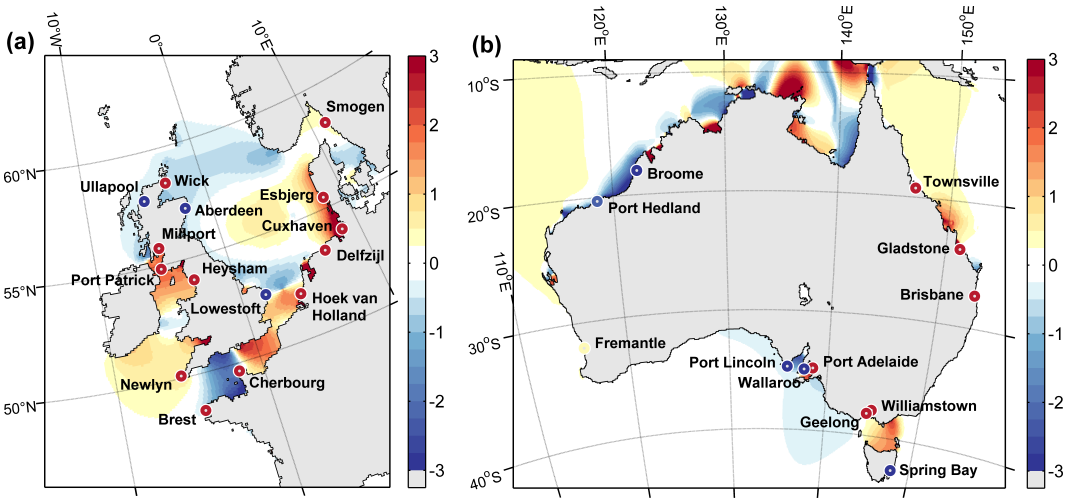

Figure 6. M_2 tidal changes (cm) as in Figure 5 but for (a) the European Shelf and (b) the coastal waters of Australia, hosting another 27 tide gauge stations.

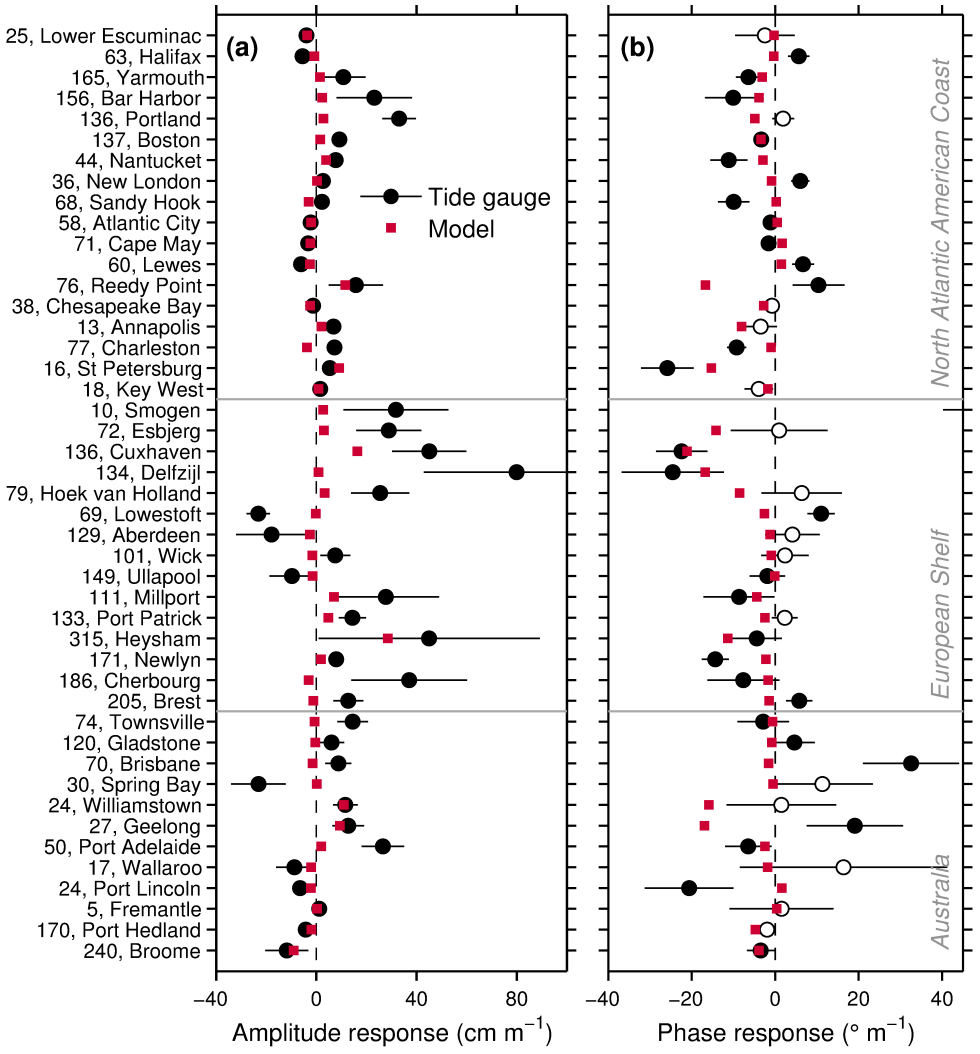

Figure 7. Observed and modeled M_2 response coefficients in (a) amplitude H and (b) phase lag G per meter of SLR. Model values are based on simulations using spatially varying depth changes averaging 0.5 m. Errorbars correspond to two standard deviations and were propagated from the trend analyses of sea level and annual tidal estimates. Stations with insignificant phase trends (at the 95% confidence level) are shown as white markers in panel (b). Numbers to the left of the station labeling indicate mean M_2 amplitudes.

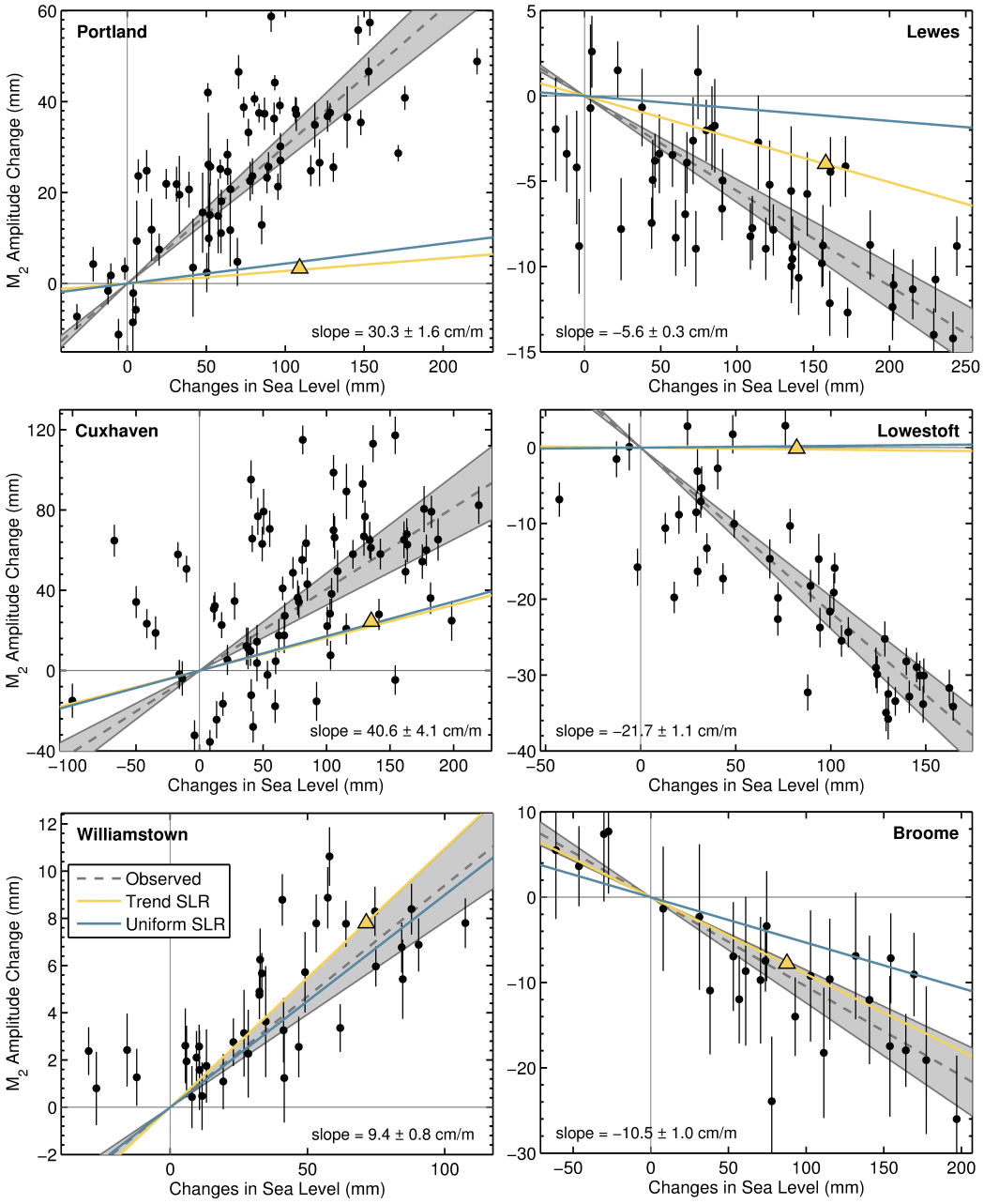

Figure 8. Regression of annual M_2 amplitude changes against mean sea level changes at six tide gauge stations. Observations (black dots with twofold standard errors) are given relative to the first data record plus residual distances to the local M_2 and sea level trends deduced in Section 4.1. Gray curves represent straight line fits to the observations and estimated uncertainties (95% confidence level) under the constraint that the lines cross the origin. Slope values at the bottom of each panel are reckoned in cm per meter of SLR. Colored lines show modeled M_2 responses for 0.5 m of uniform SLR (blue) and trend SLR (yellow), augmented by results for the 0.1 m run using trend data (yellow triangle). Neither tidal nor sea level estimates contain nodal modulations.

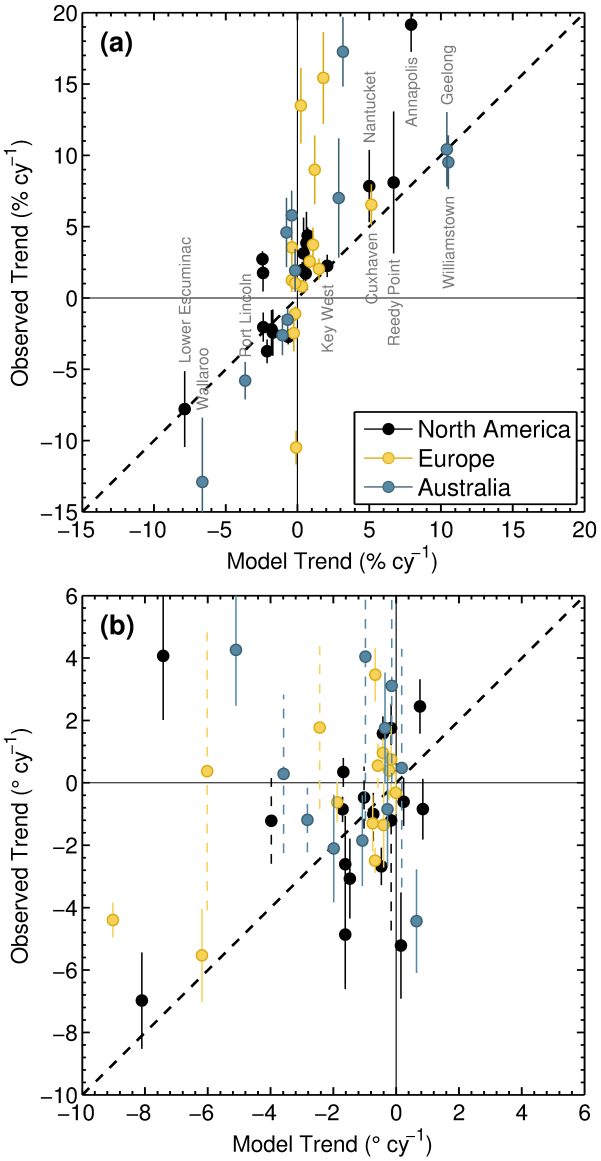

Figure 9. Comparison of observed and modeled M_2 trends in (a) relative amplitude (% cy^{-1}) and (b) phase (° cy^{-1}) at 45 tide gauge stations in North America (black markers), Europe (yellow), and Australia (blue). Stations St. Petersburg, Smogen, and Spring Bay are off the scale in panel (a); see the supporting information for respective tabulations. Errorbars of the observed tidal trends correspond to two standard deviations and are shown as dashed lines in panel (b) for stations with insignificant phase trends. Labels in (a) signify locations of particularly large model trends.

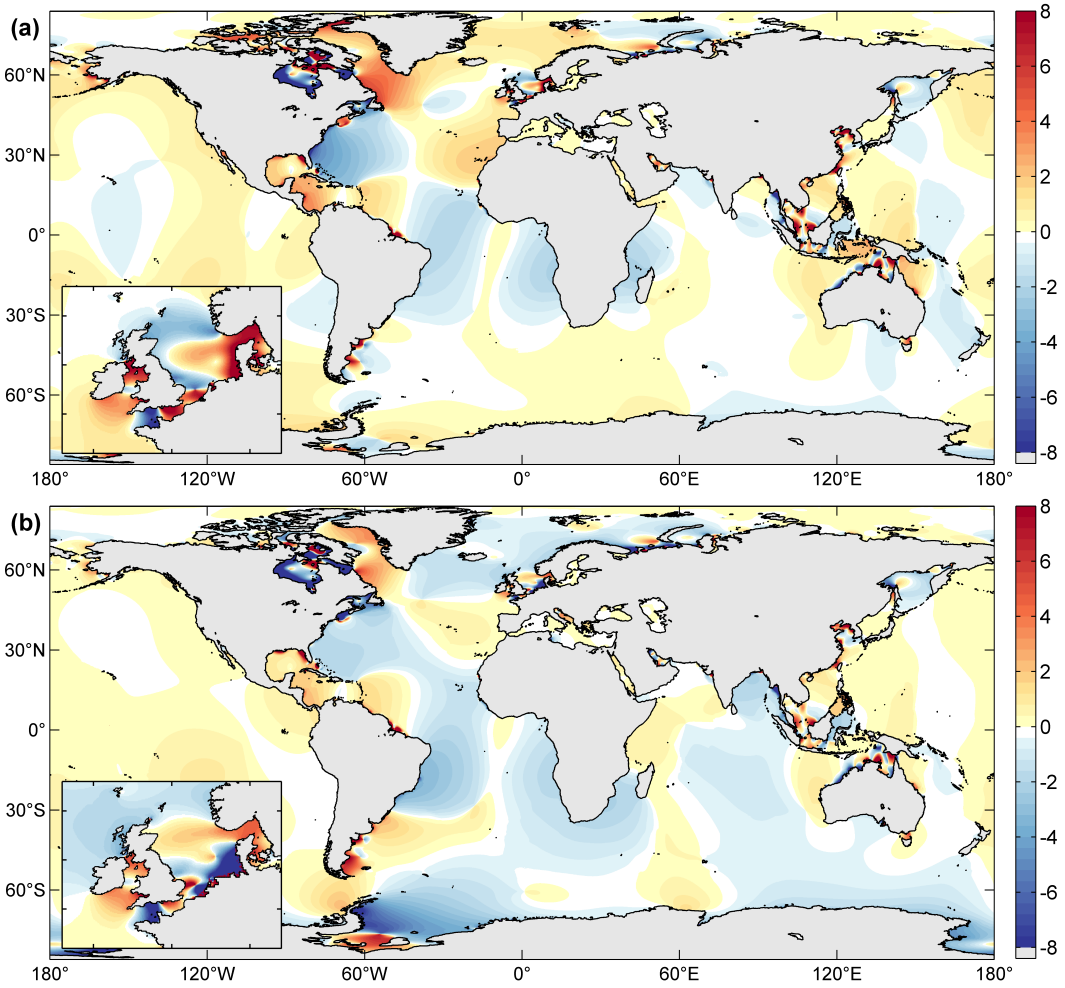

Figure 10. Change in M_2 amplitudes (cm) with an average of non-uniform SLR of 2 m, assuming (a) fixed coastlines, and (b) inundation of low-lying land. Respective close-ups of the European Shelf are shown on the bottom left of each panel.